IEEE Access
Multidisciplinary | Rapid Review | Open Access Journal

Received December 11, 2020, accepted December 16, 2020, date of publication December 24, 2020,
date of current version January 22, 2021.

Digital Object Identifier 10.1109/ACCESS.2020.3047191

An Improved Algorithm GVSPM-F for Electrical Impedance Tomography

XI HE, YU ZHANG, JIANPING LI, ZHENZHONG SONG, JIANMING WEN, JIJIE MA, AND YILI HU

Key Laboratory of Intelligent Operation and Maintenance Technology & Equipment for Urban Rail Transit of Zhejiang Province, College of Engineering, Institute of Precision Machinery and Smart Structure, Zhejiang Normal University, Jinhua 321004, China

Corresponding authors: Yu Zhang (zjnuzy@zjnu.cn) and Jianping Li (lijp@zjnu.cn)

This work was supported in part by the Natural Science Foundation of Zhejiang Province under Grant LY19E050010, Grant LY20E050009, and Grant LGF20E050001; and in part by the General Research Projects of Zhejiang Provincial Department of Education under Grant Y201943038.

ABSTRACT The generalized vector sampled pattern matching (GVSPM) algorithm is widely utilized in the EIT (electrical impedance tomography) reconstruction to solve the ill-posed inverse problem. An improved algorithm, which is called the generalized vector sampled pattern matching-fast (GVSPM-F), is proposed to improve the spatial resolution and reduce the iteration time based on the conventional GVSPM. The GVSPM merely applied the orthogonal projections to approximate the weights in the coordinate directions. The iteration of the proposed GVSPM-F algorithm is calculated in the projection direction of the space constructed by nonlinear correlated column vectors in the column space of the original sensitive matrix. Hence, the proposed GVSPM-F algorithm could achieve stable convergence without an empirical value to preserve the shape information and reduce the time consumption of GVSPM. In the experimental results, GVSPM-F is compared with the traditional GVSPM method in terms of voltage error, iteration time, and image error. The voltage error decreases by approximately 35%, and the number of iteration decreases from thousands to fewer than 100. The image error of GVSPM-F is 6% less than that of GVSPM. The proposed GVSPM-F algorithm is confirmed to be effective for the reconstruction of EIT images.

INDEX TERMS EIT, image reconstruction, GVSPM, inverse problem.

I. INTRODUCTION

Electric impedance tomography (EIT) is reconstructing the conductivity distribution by the measured surface electrical potential distribution around the target when injecting a current into the object. The surface electrical potential distribution generated by the injected current could be obtained as a solution of Laplace equation, which leads EIT to a functional tomography depending on the medium parameter and boundary condition. Thus, it is necessary to solve an inverse parameter problem to realize EIT, which is difficult due to the ill-posed inverse problem.

Compared to CT (computed tomography) and MRI (magnetic resonance imaging), EIT has its unique advantages of non-invasive, simple structures, fast imaging speed, no radiation, portable and low price. EIT has been applied in many fields such as industrial process monitoring [1]–[3], geophysical exploration [4]–[6], and biomedical diagnosis [7]–[12]. However, the image spatial resolution of EIT is limited by the complex manner in which the probing field interacts with the measured field ('soft-field' effects). The inverse model is utilized to reconstruct EIT images, and it is difficult to obtain the exact conductivity distribution for image reconstruction due to the ill-posed inverse problem. Hence, it is necessary to solve the ill-posed inverse problem to realize EIT. If the external boundary voltage conditions have a small change, the ill-posed question may make the internal conductivity data change because the electric field has low energy at the centre. The electric field is insensitive to changes in internal conductivity if the electric field has a large change at the centre, and the boundary voltage condition barely changes.

Because of the ill-posed inverse problem, it is very difficult to obtain a proper solution. Many algorithms have been proposed to solve this problem. For example. regularization techniques are used to mitigate the instability of the solutions of EIT images. One of the most widely utilized algorithms for regularization techniques is the one-step Gauss-Newton (GN)

The associate editor coordinating the review of this manuscript and approving it for publication was Wen Chen.

reconstruction algorithm [13], which enables the sophisticated regularized models to describe the EIT inverse problem through a heuristically determined prior [14], [15]. Landweber iteration algorithm is based on the steepest gradient descent method and is also widely applied in EIT [16], [17]. The algebraic reconstruction technique (ART) algorithm is a simple and effective image reconstruction method for computerized tomography and EIT [18], [19]. Other important methods include regularization via the total variation (TV) functional [20]–[22], which enables image reconstruction with edge preservation.

The generalized vector sampled pattern matching (GVSPM) algorithm [23] is an iterative algorithm, where the objective function is the angle between the normalized known vector and the normalized estimated solution of the corresponding system of equations. The key idea of the GVSPM is that the objective function is the angle obtained from the inner product between the input vector and the solution of a system of equations. GVSPM has been widely utilized to solve the ill-posed inverse problem, and it has many applications such as the images of yeast cell sedimentary distribution in a multilayered microchannel [24], solid–air two-phase flow [25], and 3D images for Perspex [26]. The recently proposed EIT research is used to monitor patients with COVID-19 [27], [28] and measure the postoperative lung volumes [29]. However, the spatial resolution of GVSPM strongly depends on the image type and iteration number. It takes thousands of iterations to obtain the ideal results, which is too much computation time. Additionally, the reconstruction image of GVSPM often cannot achieve the ideal result. To overcome some drawbacks of GVSPM, an improved algorithm GVSPM-F is proposed. GVSPM-F lets the inner product approach 1. In other words, the new algorithm lets the angle between the normalized known vector and the normalized estimated solution extremely approximate to zero. Thus, the reconstruction result will be much closer to the ideal solution.

The purpose of this study is to present a novel GVSPM-F algorithm method to achieve better spatial resolution and location accuracy. In addition, much fewer iterations are required in the reconstruction of GVSPM-F. The proof utilized the reciprocal principle to prove the linear dependence of the column space vector of a sensitive matrix. The effectiveness of the proposed algorithm is validated through comparisons with the finite element model (FEM) from Comsol and experiment results. This paper is organized as follows. In Section II, the GVSPM algorithm is introduced, and we first propose GVSPM-F. In Section III, the numerical and real data experiments are designed to simulate the situation where a disturbance is placed in the middle of a circular container. Finally, the conclusion of this paper is shown in section IV.

II. METHODS

A. GVSPM

EIT image reconstruction is based on conductivity $\boldsymbol{e}$. However, conductivity $\boldsymbol{e}$ cannot be directly measured because boundary voltage $\boldsymbol{v}$ is the measured value. Conductivity $\boldsymbol{e}$ is obtained by (1). Sensitive matrix $\boldsymbol{s}$ is calculated from Comsol. Because $\boldsymbol{s}$ is not a full rank matrix, another method to solve this problem is required, but the closest solution is also required. This is the inverse problem of EIT reconstruction. GVSPM is commonly applied to solve this problem:

$$se = v \tag{1}$$

$$v = \sum_{i=1}^{m} e_i s_i \tag{2}$$

$$e = \begin{bmatrix} e_1 & e_2 & e_3 & \cdot & e_n \end{bmatrix}^T \tag{3}$$

$$s = \begin{bmatrix} s_1 & s_2 & s_3 & \cdot & s_n \end{bmatrix} \tag{4}$$

Equation (1) illustrates the relationship between voltage and conductivity. Input vector $\boldsymbol{v}$ is represented by a linear combination of column vector $\boldsymbol{s_i}$, $\boldsymbol{i}$ = 1,2,3,...n, in sensitive matrix $\boldsymbol{s}$. The sensitive matrix is a linear mapping of the boundary voltage and internal conductivity distribution. An $m\times1$ column vector $\boldsymbol{v}$ is the measured boundary voltage, and an $n\times1$ column vector $\boldsymbol{e}$ is the conductivity of each triangle element inside; $\boldsymbol{s}$ is a regularized sensitive $m \times n$ rectangular matrix.

Normalizing by the vector 2-norm $|v|$ yields the following relationship:

$$\frac{v}{|v|} = \sum_{i=1}^{m} e_i \frac{|s_i|}{|v|} \frac{s_i}{|s_i|} = v' = s'e' \tag{5}$$

where the prime ($'$) denotes the normalized quantities.

Equation (5) implies that normalized input vector $\boldsymbol{v}'$ is obtained as a linear combination of the weighted solutions $e_i|s_i|/|v|$ with normalized column vectors $s_i/|s_i|$.

The iteration of GVSPM has the following steps:

$$e_0 = s'^T v' \tag{6}$$

$$v'_{k+1} = \frac{(s'e'_k)}{|s'e'_k|} \tag{7}$$

$$\Delta v'_{k+1} = v' - v'_{k+1} \tag{8}$$

Modification by deviation vector $\Delta\boldsymbol{v'_{k+1}}$ yields the k+1th iterative solution vector $\boldsymbol{e'_{k+1}}$ as follows:

$$e'_{k+1} = e'_k + s'^T \Delta v'_k \tag{9}$$

Exact vector $\boldsymbol{v}'$ from $\Delta\boldsymbol{v'_k}$. We deform equations (6-9) to (10):

$$e^{k+1} = e^k + s'^T \left(E - s' s^T\right) v' \tag{10}$$

where $\boldsymbol{E}$ is an $m \times m$ unit matrix.

When the inner product between $\boldsymbol{v}'$ and $\boldsymbol{s'e'}$ is 1, the angle between $\boldsymbol{s'e'}$ and $\boldsymbol{v}'$ is zero, so solution $\boldsymbol{e}$ could be obtained as:

$$f\left(e^k\right) = \frac{v}{|v|} \cdot \frac{se^k}{\left|se^k\right|} = v' \cdot s'e'^k \to 1 \tag{11}$$

If vector $\boldsymbol{v}'$ and $\boldsymbol{s'e'}$ are identical, the real solution is not necessarily solved because the solution is the conductivity.

B. GVSPM-F

The principal difference between GVSPM and GVSPM-F is illustrated in (12) and (13).

$$\text{GVSPM}: e^{k+1} = e^k + s'^T \left(E - s's^T\right) v' \tag{12}$$

$$\text{GVSPM} - \text{F}: e^{k+1} = e^k + Js'^T \left(E - s's^T\right) v' \tag{13}$$

where $\boldsymbol{J}$ is equal to $pinv(\boldsymbol{s'^T s'})\ \boldsymbol{s'^T}$, which is a self-designed matrix to simplify the equation. The reason for introducing matrix $\boldsymbol{J}$ will be explained below.

GVSPM merely applies the orthogonal projections to approximate the weights in coordinate directions $\boldsymbol{C_1}$, $\boldsymbol{C_2}$..., $\boldsymbol{C_m}$ and iteratively finds the final solution. The iteration of the proposed GVSPM-F algorithm is calculated in the projection direction of the space construct by nonlinear correlated column vectors in the column space of the original sensitive matrix. Thus, GVSPM-F could more quickly converge, and the inner product of GVSPM-F is closer to 1. Therefore, GVSPM-F could achieve better spatial resolution and less iteration time.

Equation (14) is deduced from (1) and (5).

$$s'e' = v' \tag{14}$$

Both sides of this equation produce the transpose of the sensitive matrix, which is described as follows:

$$s'^T s'e' = s'^T v' \tag{15}$$

Assuming that the sensitive matrix is full-rank, vector e′ is written as:

$$e' = \left(s'^T s'\right)^{-1} s'^T v' \tag{16}$$

In (16), if the inverse of matrix $\boldsymbol{s'^T s'}$ exists, the solution $\boldsymbol{(s'^T s')^{-1} s'^T v'}$ is not the real solution to $\boldsymbol{e}$ but the projection of vector $\boldsymbol{v'}$ onto the column space of matrix $\boldsymbol{s'}$.

The SVD is utilized for sensitive matrix $\boldsymbol{s}$, and the result is shown in (17)-(20).

$$s = U \sum V^T \tag{17}$$

where matrix $\boldsymbol{U}$ is the characteristic matrix obtained by the eigenvalue decomposition of matrix $\boldsymbol{ss^T}$; $\mathbf{V}$ is the characteristic matrix obtained by the eigenvalue decomposition of $\boldsymbol{s^T s}$;$\sum$ is a nonnegative diagonal matrix.

The pseudo-inverse of sensitive matrix $\boldsymbol{s}$ is written as:

$$s = V \sum^{-1} U^T \tag{18}$$

$$\sum = \begin{bmatrix} \delta_1 & \cdots & 0 & 0 \\ \vdots & \ddots & \vdots & \cdots\ 0 \\ 0 & \cdots & \delta_m & 0 \end{bmatrix} \tag{19}$$

$$\sum^{-1} = \begin{bmatrix} \delta_1^{-1} & \cdots & 0 \\ \vdots & \ddots & \vdots \\ 0 & \cdots & \delta_m^{-1} \\ & \vdots & \\ 0 & 0 & 0 \end{bmatrix} \tag{20}$$

We construct a function *pinv* to solve (17) and (20), which could be obtained as $pinv(\boldsymbol{s^T s})$.

In this study, sensitive matrix $\boldsymbol{s}$ is not full-rank; the rank of sensitive matrix $\boldsymbol{s}$ is less than the number of rows m. From the reciprocity theorem (which only applies to the linear resistive circuit without a controlled source), if the distance between current and sensing electrodes is similar, the difference in electrode numbers is identical, and the observation impedance is similar [30].

Because the sensitive matrix is a linear mapping of the boundary voltage to the internal potential of the field, the non-linear field is treated approximately as linear in the process of solving the forward problem. m/2 rows of the sensitive matrix are linearly independent, and the rank of the sensitive matrix is m/2. Therefore, in matrix $\sum$, the last m/2 singular values are close to zero. Because the inverse of matrix $\sum$ is $\sum^{-1}$, the last m/2 singular values of matrix $\sum^{-1}$ will become infinity. As a result, the last m/2 singular values of matrix $\sum$ must be deleted. In [31], if the last m/2 singular values to stabilize the inversion process were deleted, and all m sets of voltage data were not utilized. The point of view in our study is that the last m/2 data must be deleted due to the reciprocity theorem because m/2 rows of the sensitive matrix are linearly independent. The addition of a regularization parameter will cause errors.

We set the initial solution vector $\boldsymbol{e'_0}$ to be the orthogonal projections of known normalized vector $\boldsymbol{v}$ in the coordinate direction as (6), the iterative process of GVSPM-F is shown in (21):

$$e'_{k+1} = e'_k + pinv\left(s^T s\right) s'^T \left(v' - v'_{k+1}\right) \tag{21}$$

Here, $\boldsymbol{v'}$ is the measure boundary voltage, and $\boldsymbol{v'_{k+1}}$ is the boundary voltage calculated after each iteration.

The sensitive matrix of GVSPM-F lets the last m/2 singular values approach the zero. Therefore, the result of the pseudo-inversion to the sensitive matrix is:

$$J = pinv\left(S'^T S'\right) s'^T \tag{22}$$

The difference between GVSPM and GVSPM-F is matrix $pinv(\boldsymbol{s'^T s'})$, which implies that after the linear transformation of $pinv(\boldsymbol{s'^T s'})$, the angle $< \boldsymbol{e'_k}, \Delta\boldsymbol{e'_k} >$ is no longer almost vertical. Therefore, after the iterative convergence, the inner product between $\boldsymbol{se'_k}$ and $\boldsymbol{v'}$ will be extremely close to 1. Matrix $\boldsymbol{s'pinv(s'^T s')^{-1} s'^T}$ is the projection matrix of column vector $\boldsymbol{v}$ in the column space of sensitive matrix $\boldsymbol{s}$, and matrix $pinv(\boldsymbol{s'^T s'})\boldsymbol{s'^T}$ is the nonlinear correlation column vector's projection in the nonlinear correlation column space of the sensitive matrix. Therefore, the linear transformation of $pinv(\boldsymbol{s'^T s'})$ will substantially decrease the angle $< \boldsymbol{e'_k}, \Delta\boldsymbol{e'_k} >$. As a result, GVSPM-F has much fewer iterations than GVSPM, and the inner product between $\boldsymbol{se'_k}$ and $\boldsymbol{v'}$ is closer to 1, i.e., GVSPM-F consumes less time. In addition, the spatial resolution and location accuracy will improve.

After hundreds of thousands of iterations, the inner product of GVSPM still fails to approach 1. The reason is that

GVSPM assumes that C_1, C_2,..., C_m are orthogonal at the beginning, but this assumption is not correct, so the angle between se'_k and v' will remain relatively low as shown in Fig. 2 but cannot converge to zero. Therefore, the angle between e'_k and $\Delta e'_k$ is almost vertical as shown in Fig. 1.

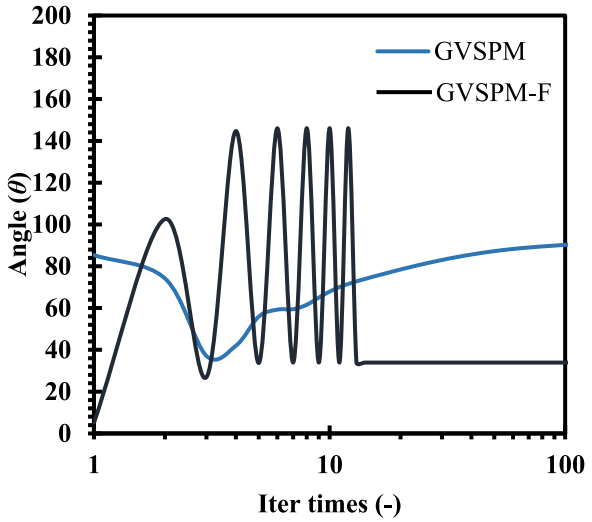

FIGURE 1. Angle between e'^k and $\Delta e'^k$.

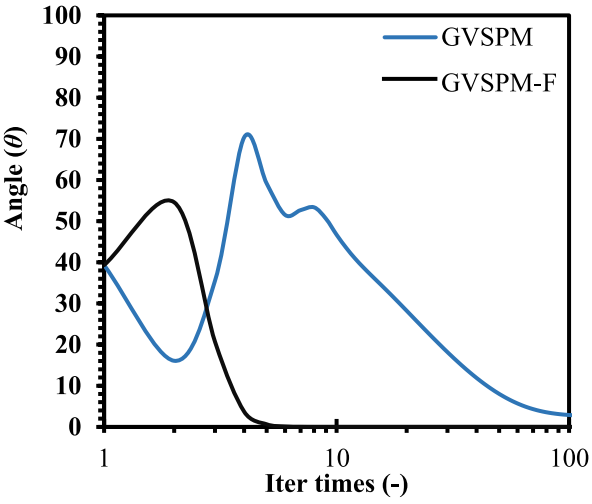

FIGURE 2. Angle between se'_k and v.

III. RESULTS

In the simulation data, there are four types of prototypes: first, a NaCl solution with a conductivity of 0.8 S/m was added to the circular area with a diameter of 90 mm, and the disturbance with a diameter of 20 mm was added to the centre; second, a 20-mm disturbance is placed in the lower-left portion of a 90-mm-diameter circle filled with NaCl solution; third, a 20-mm-diameter disturbance was placed in the middle, and two 10-mm-diameter disturbances were placed on each side of the 45-degree inclination; fourth, three circular disturbances with diameters of 20 mm were placed at three locations in a triangular shape. For each current injection, the voltages were obtained by solving the Poisson equation using the finite-element method.

A. SIMULATION RESULTS

To objectively evaluate the image quality in the simulation results and experiment result, image error I_e is a common coefficient to evaluate the image quality, which is calculated as:

$$I_e = \frac{\sqrt{\sum_{j=1}^{N}\left(\sigma_j^k - \sigma_j^{ori}\right)}}{\sqrt{\sum_{j=1}^{N}\sigma_j^{ori}}} \tag{23}$$

where σ_j^k is the jth element after k iterations of the reconstructed image; σ_j^{ori} is the jth element of the original image conductivity; N is the pixel number of the image. A lower value of I_e indicates better image quality.

Fig. 3(a) shows the simulation prototype with a circle distribution at the centre of the circular tank. Figs. 3(b-d) show the GVSPM reconstruction results after 10, 100, and 1000 iterations. Figs. 3(e-g) show the GVSPM-F reconstruction results after 10, 100, and 1000 iterations.

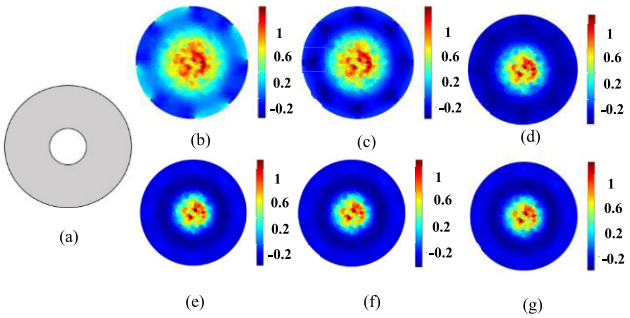

FIGURE 3. Result of the disturbance at the centre and different Iteration results of GVSPM and GVSPM-F: (a) Original conductivity distribution; (b-d) GVSPM result (with 10, 100, 1000 iterations); (e-g) GVSPM-F result. (with 10, 100, 1000 iterations).

Considering the GVSPM and GVSPM-F results in Fig. 3, GVSPM-F has a better spatial resolution and location accuracy with the most significant difference in the result of 10 iterations. After 10 iterations, the reconstruction results of GVSPM-F converged. Therefore, there is almost no change from Fig. 3(e) to Fig. 3(g). The reconstruction results of GVSPM-F obtain better location accuracy when the number of iterations increases.

In Table 1, the image error of GVSPM widely fluctuates between 0.983-0.972 with the lowest point of 0.972 at 30 iterations. The image error of GVSPM-F begins at 0.974 and dramatically decreases to approximately 0.952; then, the image value of GVSPM-F remains steady.

Based on Fig. 3, the reconstruction results of GVSPM-F have better location accuracy and spatial resolution. Furthermore, GVSPM-F could converge in only eight iterations. Based on Table 1, GVSPM-F has a lower image error than GVSPM, so the results of GVSPM-F reconstruction are more stable and accurate.

TABLE 1. Image error with the disturbance at the centre.

Iteration times	Image error of GVSPM	Image error of GVSPM-F
1	0.9834	0.9742
3	0.9822	0.9654
8	0.9803	0.9523
10	0.9788	0.9523
30	0.9723	0.9523
50	0.9736	0.9523
100	0.9756	0.9523
500	0.9731	0.9523
1000	0.981	0.9523

TABLE 2. Image error with the disturbance at the lower left centre of the circle.

Iteration times	Image error of GVSPM	Image error of GVSPM-F
1	0.9853	0.9883
3	0.9842	0.9801
8	0.984	0.9711
10	0.9829	0.9701
30	0.9827	0.9702
50	0.9826	0.9701
100	0.9814	0.9701
500	0.9805	0.9701
1000	0.9808	0.9701

The simulation prototype with a circle distribution in the north-west side of the circular tank is shown in Fig. 4(a). Figs. 4(b-d) show the GVSPM reconstruction results after 10, 100, and 1000 iterations. Figs. 4(e-g) show the GVSPM-F reconstruction results after 10, 100, and 1000 iterations.

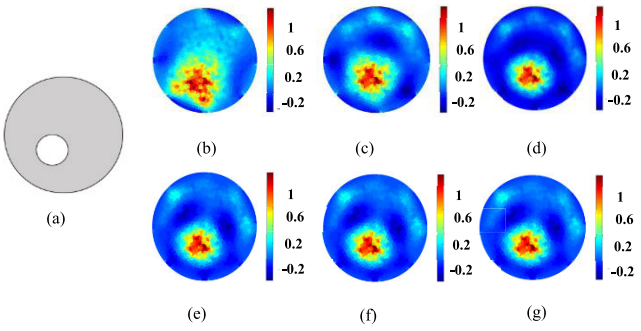

FIGURE 4. Result of the disturbance moving towards the lower left centre of the circle and different Iteration results of GVSPM and GVSPM-F: (a) Original conductivity distribution; (b-d) GVSPM result (10, 100, 1000 iterations); (e-g) GVSPM-F result.

From Fig. 4(b) to Fig. 4(d), the images become clearer and approach the shape of the original simulation result. However, the reconstruction image of GVSPM after 1000 iterations is still worse than the reconstruction image of GVSPM-F after 10 iterations.

The image errors of GVSPM and GVSPM-F follow similar trends: they begin at 0.985 and 0.988, respectively, and decrease. GVSPM-F remains steady after 10 iterations. The image error of GVSPM-F decreases throughout the entire period.

Overall, the image of GVSPM-F has better spatial resolution and location accuracy than GVSPM. In addition, GVSPM-F could converge faster.

Fig. 5 (a) illustrates the third prototype, where a disturbance with a diameter of 20 mm is placed in the middle, and two smaller disturbances with diameters of 10 mm are on each side of the 45-degree inclination.

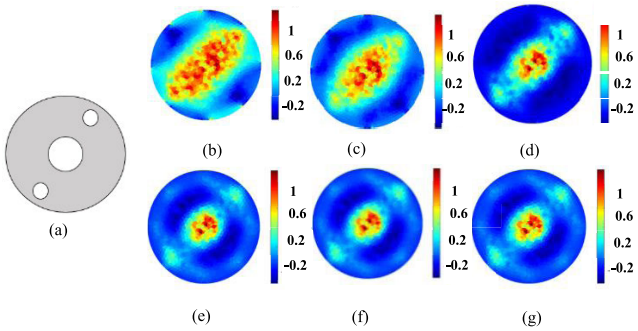

FIGURE 5. Result of the disturbance at the centre and two smaller disturbances at the top of the slope on either side. Different Iteration results of GVSPM and GVSPM-F: (a) Original conductivity distribution; (b-d) GVSPM result (10, 100, 1000 iterations); (e-g) GVSPM-F result.

TABLE 3. Image error with the disturbance at the centre and smaller disturbances at the top of the slope on either side.

Iteration times	Image error of GVSPM	Image error of GVSPM-F
1	0.9924	0.9943
3	0.9893	0.9871
8	0.978	0.9636
10	0.9775	0.9636
30	0.9773	0.9634
50	0.9771	0.9635
100	0.976	0.9634
500	0.9786	0.9633
1000	0.9804	0.9633

In Fig. 5, the original simulation result has three circular disturbances. The result of GVSP-F has a clear image of approximately three circles after only 10 iterations. However, the result of GVSPM appears similar to a rectangle disturbance. After the iteration, the results of GVSPM are clearer with the increase in the number of iterations, but the results of GVSPM-F are clearer and more accurate.

The image error of GVSPM-F consistently decreases to 0.963 in 8 iterations and remains stable over the remaining

period. Similarly, GVSPM begins at approximately 0.992, after which GVSPM begins to decline to 0.976 and then slightly increase to 0.980 at 1000 iterations. The lowest image errors of GVSPM and GVSPM-F are 0.976 and 0.963, respectively, so GVSPM-F has a better reconstruction image than GVSPM.

In Fig. 6(a), there are three disturbances. We place three circle disturbances at 120 degrees.

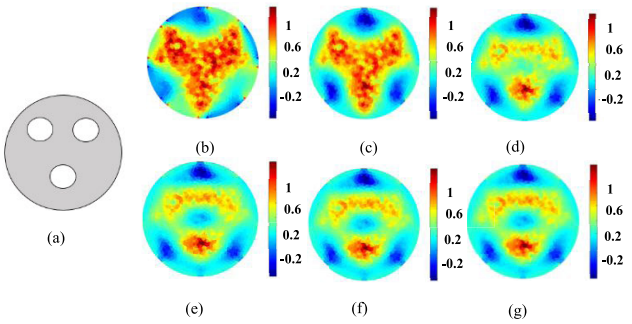

FIGURE 6. Three disturbances in the circuit; different Iteration results of GVSPM and GVSPM-F: (a) Original conductivity distribution; (b-d) GVSPM result (10, 100, 1000 iterations); (e-g) GVSPM-F result.

TABLE 4. Image error with three disturbances in the circuit.

Iteration times	Image error of GVSPM	Image error of GVSPM-F
1	0.9878	0.9663
3	0.9843	0.9616
8	0.9833	0.9576
10	0.9817	0.9576
30	0.9815	0.9576
50	0.9813	0.9576
100	0.981	0.9576
500	0.9811	0.9576
1000	0.9792	0.9576

Figs. 6(b-d) show the results of GVSPM; there is no disturbance at the centre of the circle. However, the reconstruction image of GVSPM looks similar to a triangle.

The image errors of GVSPM and GVSPM-F begin at 0.988 and 0.966, respectively; then, both continue to decrease to 0.979 and 0.958. The image error of GVSPM is approximately 0.3 higher than that of GVSPM-F.

In conclusion, from all simulation results, the reconstruction results of GVSPM-F could use much less time to converge, and the inner product is much closer to 1 than GVSPM. Larger inner products imply that the reconstruction result is closer to the ideal solution. Furthermore, using GVSPM-F to reconstruct the image could greatly improve the location accuracy and spatial resolution with very few iterations.

As the number of higher conductivity circular area increases, the results become worse for both methods. The reason for that is because the reconstruction accuracy of EIT will naturally decrease as the complexity of the probing field increases. Because that more complex probing field means that there are more errors in the inverse problem. The reconstruction accuracy of EIT is limited by the complex manner. This is known as 'soft-field' effects (the probing field interacts with the measurand) [1].

B. EXPERIMENTAL RESULT

The measurement object of experiments is the glass rod. The applied alternate current is $\boldsymbol{i_c} = 0.1$ mA. The frequencies of applied current are $f = 50$ kHz. The resolution of the reconstructed image N is 2042.

1) EXPERIMENTAL SETUP

As shown in Fig. 7, the experimental setup is based on Red-Pitaya platform, which integrates a System-on-Chip (SoC) Zynq-7010 (Xilinx, Inc., San Jose, CA). The SoC combines an ARM dual-core Cortex-A9 MPCore processor with an FPGA. The system consists of a signal generator (RIGOL DG4162), a power amplifier (Tabor Electronic FCHVWA 9400), a power supply, a gating switch, a red pitaya, and a laptop computer.

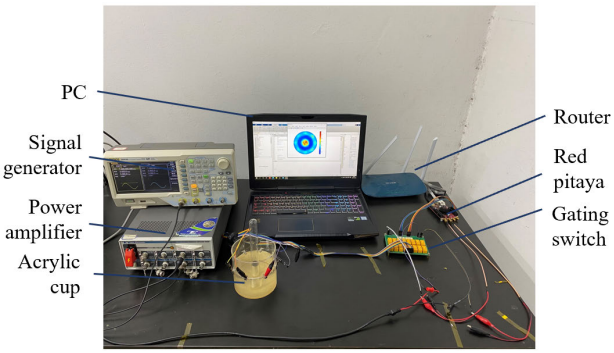

FIGURE 7. EIT instrument; cables connect the data acquisition system to a laptop computer.

2) EXPERIMENTAL RESULTS

Another coefficient to evaluate the image quality is voltage error $U_{\mathrm{e},}$, which is calculated as:

$$U_{\mathrm{e}} = \frac{\sqrt{\sum_{i=1}^{M}\left(u_i^k - u_i^{ori}\right)}}{\sqrt{\sum_{j=1}^{N} u_j^{ori}}} \tag{24}$$

where i is the ith measurement number; M is the total number of measurements; $u_{\mathrm{j}}^{\mathrm{k}}$ is the j th element of the final iterative potential, which is calculated from the final k = K iterative reconstructed image; $u_{\mathrm{j}}^{\mathrm{ori}}$ is the ith measured voltage from experiments; U_{e} quantifies the difference between $u_{\mathrm{j}}^{\mathrm{k}}$ and $u_{\mathrm{j}}^{\mathrm{ori}}$. A smaller value of U_{e} implies better image quality.

Figs. 8(a-d) show the experiment results of GVSPM with 10, 100, 1000, and 5000 iterations. Figs. 8(e-g) illustrates the experiment results of GVSPM-F with 10, 100, and 1000 iterations. The reconstruction image of GVSPM-F achieves better image quality, and the artefacts of eight electrodes become increasingly clearer with more iterations. However, the artefact of eight electrodes does not reflect that the image worsens

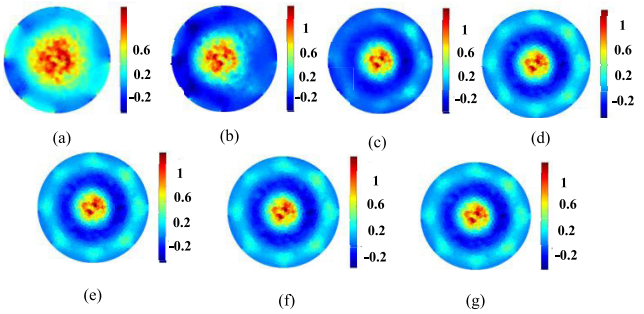

FIGURE 8. Different Iteration results of GVSPM: (a-d) GVSPM-F (a-d) GVSPM results (Iterate 10, 100, 1000, 5000 times) and (e-g) GVSPM-F results. A glass rod is placed in a circular tank.

after more iterations because the image with artefacts is the real situation.

Table 5 clearly shows that the image errors of GVSPM and GVSPM-F begin at almost identical recorded values. The image error of GVSPM slightly fluctuates and remains relatively high throughout the entire period, while the image error of GVSPM-F dramatically drops to 0.922 at 10 iterations and remains steady.

TABLE 5. Image error of experiment results.

Iteration times	Image error of GVSPM	Image error of GVSPM-F
1	0.9796	0.9843
3	0.9801	0.9796
8	0.9803	0.9423
10	0.9801	0.9221
30	0.9763	0.9221
50	0.9802	0.9221
100	0.9778	0.9221
500	0.9807	0.9223
1000	0.9738	0.9221

In Fig. 9, figures (1-4) are the voltage error of 4 different simulations, and figure (5) is the experiment result. Minimum voltage error U_e of these reconstruction results is 0.4936, 0.5029, 0.4982, 0.4951, and 0.5386. GVSPM-F converges after the 8th iteration, and the minimum voltage error U_e of GVSPM-F is 0.1449, 0.2364, 0.2357, 0.2350, and 0.2618. Compared to the results of GVSPM and GVSPM-F, the voltage errors of GVSPM-F results are 35% lower than the results of GVSPM on average, which implies that the reconstruction image of GVSPM-F has better image quality.

In the experiment result, the inner product of GVSPM-F between $\boldsymbol{s}'\boldsymbol{e}'^{\mathbf{k}}$ and $\boldsymbol{v}$ converges to 0.9835 after only 9 iterations. After 1000 iterations, the inner product of GVSPM reaches 0.9567. Finally, the GVSPM inner product results converge to 0.9635. The inner product of this experiment result could not more closely approach 1 because this method utilizes all voltage data, but the voltage data have a nose error. The voltage data do not satisfy the reciprocity theorem, so all voltage data are linearly independent. Thus, not all voltage data will converge in the iteration because the eigenvalue of

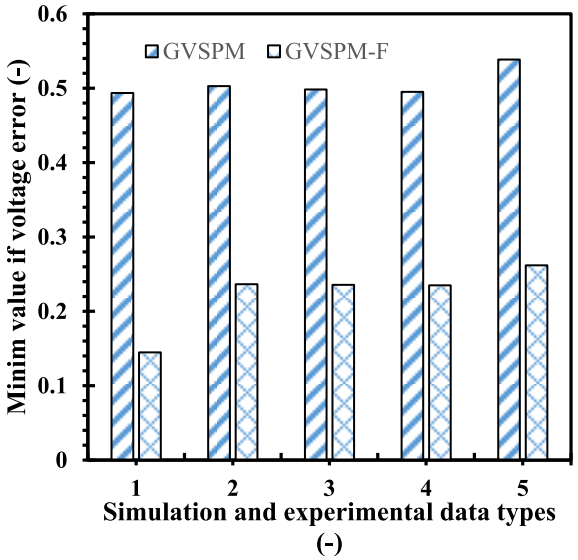

FIGURE 9. The minimum value of U_e, which is calculated by GVSPM and GVSPM-F. (1-4) The contrast between GVSPM and GVSPM-F in the first of four simulation results. (5) The contrast between GVSPM and GVSPM-F in the experimental result.

transfer matrix λ is not always less than 1, and it will not converge at the end of every iteration of the measurement.

In conclusion, GVSPM is a powerful iterative solver for any ill-posed linear system equations. It enables us to obtain reliable and stable solutions for EIT reconstruction. to improve the resolution of EIT images. Most of the calculation time of GVSPM-F is spent on the pseudo-inverse calculation of matrix $\boldsymbol{s}'$, which can be calculated before the iterative algorithm, and then the calculation time gap between GVSPM and GVSPM-F will be huge.

IV. CONCLUSION

The objective of this paper is to develop a novel algorithm based on the GVSPM algorithm to enhance the EIT image reconstruction by linear dependence column space vectors of a sensitive matrix during iteration. Compared to the GVSPM algorithm, the proposed method achieves a higher spatial resolution and less iteration time. The image error of GVSPM-F is 6% less than that of GVSPM. The voltage error decreases by approximately 35% and the number of iterations decreases from thousands to fewer than 100. We established the relationship between the reciprocal theorem and the EIT inverse problem. In addition, there is only half of the independent measure data. Hence, the acquisition time could be reduced by half.

The major advantage of GVSPM-F is that GVSPM-F converges much faster than GVSPM. Because the inner product of GVSPM-F is much closer to 1 after convergence. As a result, GVSPM-F could achieve better location accuracy and spatial resolution. However, GVSPM-F still has a problem that the change of inner product is much larger than GVSPM for each step. Therefore, some inner product results may be missed. In most situations, the closer the inner product gets

to 1, the better the image result could get, and GVSPM-F could obtain the inner product which is closer to 1 than the result of GVSPM.

REFERENCES

[1] H. S. Tapp, A. J. Peyton, E. K. Kemsley, and R. H. Wilson, "Chemical engineering applications of electrical process tomography," *Sens. Actuators B, Chem.*, vol. 92, nos. 1–2, pp. 17–24, Jul. 2003.

[2] A. Seppänen, A. Voutilainen, and J. P. Kaipio, "State estimation in process tomography—Reconstruction of velocity fields using EIT," *Inverse Prob.*, vol. 25, no. 8, p. 085009, Jul. 2009.

[3] J. Jia, M. Wang, H. I. Schlaberg, and H. Li, "A novel tomographic sensing system for high electrically conductive multiphase flow measurement," *Flow Meas. Instrum.*, vol. 21, no. 3, pp. 184–190, Sep. 2010.

[4] P. Church, J. E. Mcfee, S. Gagnon, and P. Wort, "Electrical impedance tomographic imaging of buried landmines," *IEEE Trans. Geosci. Remote Sens.*, vol. 44, no. 9, pp. 2407–2420, Sep. 2006.

[5] E. Zimmermann, A. Kemna, J. Berwix, W. Glaas, and H. Vereecken, "EIT measurement system with high phase accuracy for the imaging of spectral induced polarization properties of soils and sediments," *Meas. Sci. Technol.*, vol. 19, no. 9, Jul. 2008, Art. no. 094010.

[6] G. Bouchette, P. Church, J. E. Mcfee, and A. Adler, "Imaging of compact objects buried in underwater sediments using electrical impedance tomography," *IEEE Trans. Geosci. Remote Sens.*, vol. 52, no. 2, pp. 1407–1417, Feb. 2014.

[7] H. Ma, H. Li, X. Liu, W. Li, J. Xia, B. Liu, X. Shi, X. Dong, and F. Fu, "Real-time monitoring of contact impedance from multiple electrode–scalp interfaces during cerebral electrical impedance tomography," *IEEE Access*, vol. 7, pp. 95186–95196, 2019.

[8] G. Ma and M. Soleimani, "Spectral capacitively coupled electrical resistivity tomography for breast cancer detection," *IEEE Access*, vol. 8, pp. 50900–50910, Mar. 2020.

[9] H. Li, L. Cao, C. Xu, B. Yang, M. Dai, X. Shi, X. Dong, and F. Fu, "Evaluating and reducing the influence of scalp dehydration in the monitoring of intracranial dehydration using electrical impedance tomography," *IEEE Access*, vol. 8, pp. 105047–105054, 2020.

[10] T. Tidswell, A. Gibson, R. H. Bayford, and D. S. Holder, "Three-dimensional electrical impedance tomography of human brain activity," *NeuroImage*, vol. 13, no. 2, pp. 283–294, Feb. 2001.

[11] M. T. Clay and T. C. Ferree, "Weighted regularization in electrical impedance tomography with applications to acute cerebral stroke," *IEEE Trans. Med. Imag.*, vol. 21, no. 6, pp. 629–637, Jun. 2002.

[12] R. J. Halter, A. Hartov, and K. D. Paulsen, "A broadband high-frequency electrical impedance tomography system for breast imaging," *IEEE Trans. Biomed. Eng.*, vol. 55, no. 2, pp. 650–659, Feb. 2008.

[13] A. Adler and R. Guardo, "Electrical impedance tomography: Regularized imaging and contrast detection," *IEEE Trans. Med. Imag.*, vol. 15, no. 2, pp. 170–179, Apr. 1996.

[14] J. P. Kaipio, V. Kolehmainen, M. Vauhkonen, and E. Somersalo, "Inverse problems with structural prior information," *Inverse Problems*, vol. 15, no. 3, pp. 713–729, Jun. 1999.

[15] Y. Yang, J. Jia, N. Polydorides, and H. McCann, "Effect of structured packing on EIT image reconstruction," in *Proc. IEEE Int. Conf. Imag. Syst. Techn. (IST)*, Santorini, Greece, Oct. 2014, pp. 53–58.

[16] W.-Q. Yang, D. M. Spink, T. A. York, and H. McCann, "An image-reconstruction algorithm based on Landweber's iteration method for electrical-capacitance tomography," *Meas. Sci. Technol.*, vol. 10, no. 11, pp. 1065–1069, Nov. 1999.

[17] H. Wang, C. Wang, and W. Yin, "A pre-iteration method for the inverse problem in electrical impedance tomography," *IEEE Trans. Instrum. Meas.*, vol. 53, no. 4, pp. 1093–1096, Aug. 2004.

[18] T. Li, T.-J. Kao, D. Isaacson, J. C. Newell, and G. J. Saulnier, "Adaptive kaczmarz method for image reconstruction in electrical impedance tomography," *Physiol. Meas.*, vol. 34, no. 6, pp. 595–608, May 2013.

[19] Y. Z. Ider and S. Onart, "Algebraic reconstruction for 3D magnetic resonance–electrical impedance tomography (MREIT) using one component of magnetic flux density," *Physiol. Meas.*, vol. 25, no. 1, pp. 281–294, Feb. 2004.

[20] A. Borsic, B. M. Graham, A. Adler, and W. Lionheart, "*In vivo* impedance imaging with total variation regularization," *IEEE Trans. Med. Imag.*, vol. 29, no. 1, pp. 44–54, Jan. 2010.

[21] Z. Zhou, G. S. dos Santos, T. Dowrick, J. Avery, Z. Sun, H. Xu, and D. S. Holder, "Comparison of total variation algorithms for electrical impedance tomography," *Physiol. Meas.*, vol. 36, no. 6, pp. 1193–1209, May 2015.

[22] W. Shang, W. Xue, Y. Li, and Y. Xu, "Improved primal–dual interior-point method using the lawson-norm for inverse problems," *IEEE Access*, vol. 8, pp. 41053–41061, Feb. 2020.

[23] G. Y. Dong, H. Endo, S. Hayano, S. K. Gao, and Y. Saito, "GVSPM for reconstruction in electrical impedance tomography," *IEEE Trans. Magn.*, vol. 39, no. 3, pp. 1630–1633, May 2003.

[24] X. Liu, J. Yao, T. Zhao, H. Obara, Y. Cui, and M. Takei, "Image reconstruction under contact impedance effect in micro electrical impedance tomography sensors," *IEEE Trans. Biomed. Circuits Syst.*, vol. 12, no. 3, pp. 623–631, Jun. 2018.

[25] M. Takei and Y. Saito, "Application of the generalized vector sampled pattern matching method to reconstruction of electrical capacitance CT images," *Meas. Sci. Technol.*, vol. 15, no. 7, pp. 1371–1381, Jun. 2004.

[26] G. Dong, R. H. Bayford, S. Gao, Y. Saito, R. Yerworth, D. Holder, and W. Yan, "The application of the generalized vector sample pattern matching method for EIT image reconstruction," *Physiol. Meas.*, vol. 24, no. 2, pp. 449–466, Apr. 2003.

[27] P. V. D. Zee, P. Somhorst, H. Endeman, and D. Gommers, "Electrical impedance tomography for positive end-expiratory pressure titration in COVID-19 related ARDS," *Amer. J. Respiratory Crit. Care Med.*, vol. 202, pp. 280–284, Jul. 2020.

[28] Y. Fu, R. Zou, S. Wang, J. Wen, L. Rong, M. Tang, B. Yu, F. Cen, Z. Zhao, I. Frerichs, A. Adler, Y. Liu, and L. Liu, "Monitoring bronchoalveolar lavage with electrical impedance tomography: First experience in a patient with COVID-19," *Physiol. Meas.*, vol. 41, no. 8, Sep. 2020, Art. no. 085008.

[29] J. Park, E.-K. Lee, J.-H. Lee, E. J. Oh, and J. J. Min, "Effects of inspired oxygen concentration during emergence from general anaesthesia on postoperative lung impedance changes evaluated by electrical impedance tomography: A randomised controlled trial," *J. Clin. Monitor. Comput.*, vol. 34, no. 5, pp. 995–1004, Oct. 2020.

[30] T. Yamaguchi, K. Maki, and M. Katashima, "Practical human abdominal fat imaging utilizing electrical impedance tomography," *Physiol. Meas.*, vol. 31, no. 7, pp. 963–978, Jun. 2010.

[31] G. Dong, H. Liu, R. H. Bayford, R. Yerworth, S. Gao, D. Holder, and W. Yan, "The spatial resolution improvement of EIT images by GVSPM-FOCUSS algorithm," *Physiol. Meas.*, vol. 25, no. 1, pp. 209–225, Feb. 2004.

XI HE was born in Sichuan, China, in 1999. He received the bachelor's degree from the School of Engineering, Zhejiang Normal University, Jinhua, China, in 2018.

Since 2019, he has been working with Zhejiang Normal University. His current research interest includes electrical impedance tomography in biomedical science.

YU ZHANG was born in Zhejiang, China, in 1979. He received the B.E. and M.E. degrees from the School of Mechanical Science and Engineering, Changsha University of Science & Technology, Changsha, China, in 2000 and 2005, respectively, and the Ph.D. degree from the School of Mechanical Science and Engineering, Tongji University, Shanghai, China, in 2009. Since 2009, he has been working with the Institute of Precision Machinery and Smart Structure, College of Engineering, Zhejiang Normal University. His current research interests include the application of electrical impedance spectroscopy in biomedical science and embedded controls in mechanical engineering.

JIANPING LI was born in Jiangsu, China, in 1987. He received the B.S. and Ph.D. degrees from the School of Mechanical Science and Engineering, Jilin University, Changchun, China, in 2011 and 2016, respectively.

After that, he worked at Chiba University, Japan, as a JSPS Researcher, supported by the Japan Society for the Promotion of Science (JSPS). In 2018, he come back to China, and has been working with the Institute of Precision Machinery and Smart Structure, College of Engineering, Zhejiang Normal University, since 2018. His current research interests include piezoelectric actuator-based nano-positioning systems, and the application of electrical impedance spectroscopy in biomedical science.

ZHENZHONG SONG was born in Guizhou, China, in 1996. He is currently pursuing the bachelor's degree with Zhejiang Normal University, Jinhua, China, where he started working with the Institute of Precision Machinery and Smart Structure, College of Engineering. His current research interests electrical impedance tomography in biomedical science.

JIANMING WEN was born in 1980. He received the B.Sc., M.Sc., and Ph.D. degrees from Jilin University, in 2003, 2006, and 2009, respectively. He is currently a Professor with Zhejiang Normal University, China. He has published more than 40 scientific articles. His main research interests include piezoelectric drive and control technology.

JIJIE MA received the B.Sc. degree in automation from Dalian Maritime University, China, in 2003, and the M.S. and Ph.D. degrees in mechanical engineering from Jilin University, China, in 2006 and 2010, respectively. He has been a Lecturer with Zhejiang Normal University. He has published more than ten scientific articles. His main research interest includes precision machinery.

YILI HU was born in Hangzhou, China, in 1989. He received the B.S. degree in mechanical design, manufacturing, and automation, and the M.S. degree in physical electronics from Zhejiang Normal University, Jinhua, China, in 2008 and 2012, respectively, and the Ph.D. degree from Shanghai Jiao Tong University, Shanghai, China, in 2020.

He is currently working as a Lecturer with Zhejiang Normal University. His current research interests include piezoelectric actuators, sensors, and energy harvesters.